

POLARIMETRIC ANALYSIS OF THE LONG DURATION GAMMA RAY BURST GRB 160530A WITH THE BALLOON BORNE COMPTON SPECTROMETER AND IMAGER

A.W. LOWELL, S.E. BOGGS, C.L. CHIU, C.A. KIERANS, C. SLEATOR, J.A. TOMSICK, A.C. ZOGLAUER,¹
H.-K. CHANG, C.-H. TSENG, C.-Y. YANG,² P. JEAN, P. VON BALLMOOS,³ C.-H. LIN,⁴ AND M. AMMAN⁵

¹*Space Sciences Laboratory, University of California, Berkeley, USA*

²*Institute of Astronomy, National Tsing Hua University, Taiwan*

³*IRAP Toulouse, France*

⁴*Institute of Physics, Academia Sinica, Taiwan*

⁵*Lawrence Berkeley National Laboratory, USA*

ABSTRACT

A long duration gamma-ray burst, GRB 160530A, was detected by the Compton Spectrometer and Imager (COSI) during the 2016 COSI Super Pressure Balloon campaign. As a Compton telescope, COSI is inherently sensitive to the polarization of gamma-ray sources in the energy range 0.2-5.0 MeV. We measured the polarization of GRB 160530A using 1) a standard method (SM) based on fitting the distribution of azimuthal scattering angles with a modulation curve, and 2) an unbinned, maximum likelihood method (MLM). In both cases, the measured polarization level was below the 99% confidence minimum detectable polarization levels of $72.3 \pm 0.8\%$ (SM) and $57.5 \pm 0.8\%$ (MLM). Therefore, COSI did not detect polarized gamma-ray emission from this burst. Our most constraining 90% confidence upper limit on the polarization level was 46% (MLM).

Keywords: balloons — instrumentation: polarimeters — gamma rays: general — gamma-ray burst:
individual (GRB 160530A) — polarization — techniques: polarimetric

1. INTRODUCTION

Decades of broad band observations of gamma-ray bursts (GRBs) have shed light on the nature of GRBs and their progenitors. Despite this, there are still significant gaps in our understanding of the GRB prompt gamma-ray emission. In particular, the emission mechanism, emission geometry, and magnetic field structure of the inner GRB jet are currently not well understood. A major challenge that any model for the GRB prompt emission faces is reconciling the spectral and temporal diversity that is seen across the GRB population. It is believed that polarization measurements, taken together with spectra and light curves, have the potential to significantly further our understanding of the GRB prompt emission.

Various scenarios have been proposed which can yield a net linear polarization of the prompt emission, as measured by a distant observer (Toma et al. 2009). Synchrotron emission is often invoked as the emission mechanism, which can produce high levels of polarization when an ordered, large-scale magnetic field exists in the jet and the viewing angle happens to fall within the jet cone (Lyutikov et al. 2003; Granot 2003). If the magnetic field is randomly oriented over small length scales throughout the jet, then a high level of polarization can only be seen when the viewing angle aligns with the edge of the jet, due to a loss of symmetry (Gruzinov & Waxman 1999; Waxman 2003). Likewise, inverse Compton emission can yield high levels of linear polarization, but only when the viewing angle is near the jet edge (Shaviv & Dar 1995; Lazzati et al. 2004). In general, each scenario can yield a range of polarization levels which depends on the observer viewing angle, as well as jet opening angle, the Lorentz factor of the burst, spectral parameters, etc. Therefore, in order to discriminate between models, a statistical analysis of a large sample of GRB polarization measurements is required (Toma et al. 2009).

To date, only a limited number of GRB prompt emission polarization measurements exist, with detection significances ranging from $\sim 1.5-4\sigma$ (McConnell 2017). Most of these measurements were carried out with instruments that were not optimized or calibrated to perform gamma-ray polarimetry. One exception is IKAROS/GAP (Yonetoku et al. 2011a), a dedicated GRB polarimeter aboard the JAXA solar sail IKAROS which is responsible for the most significant GRB polarization measurements to date (Yonetoku et al. 2012). The POLAR instrument aboard the Chinese space station Tiangong 2 is another dedicated GRB polarimeter which was only recently deployed (Sun et al. 2016; Orsi et al. 2014; Produit et al. 2005). POLAR has successfully detected several GRBs in its few months of service (Kole & Marcinkowski 2016; Kole et al. 2016), although no polarization analyses have yet been published. Most recently, the Astrosat/CZTI team (Bhalerao et al. 2017) has reported GRB polarization measurements for eleven bright GRBs with detection significances ranging from 2.5σ to less than 4σ (Chattopadhyay et al. 2017).

The Compton Spectrometer and Imager (COSI) is a 0.2-5.0 MeV gamma-ray Compton imager, spectrometer, and polarimeter developed under the NASA APRA program to fly on NASA's newly developed 18 million cubic feet Super Pressure Balloon (SPB) (Chiu et al. 2015; Kierans et al. 2017). COSI combines a wide field of view, 3D positioning, and high spectral resolution in order to address a number of science targets, including GRB polarization. Here we report the COSI detection of the bright, long-duration GRB 160530A and the associated polarimetric analysis for this GRB.

2. THE COMPTON SPECTROMETER AND IMAGER

The COSI detector system is comprised of a $2 \times 2 \times 3$ array of high-purity germanium double-sided strip detectors (GeDs) (Amman et al. 2007) surrounded by a scintillating cesium iodide (CsI) anti-coincidence shield (ACS). Each GeD measures 8 cm on a side and 1.5 cm thick, with the electrodes on each side segmented into 37 strips. 3D positioning in the GeDs is achieved by identifying the x and y strips that triggered on each side of the detector, and then converting the time difference between the x and y signals to infer the depth, or z coordinate (Lowell et al. 2016). The position resolution in the x and y directions is equal to the strip pitch, which is 2 mm. Along the z direction, the position resolution is pixel dependent, as it depends primarily on electronic noise, but on average is 0.2 mm rms. High spectral resolution is achieved by virtue of using germanium as the detector material, with an average energy resolution of 2.7 keV at 662 keV per channel.

An ideal photon event consists of at least one Compton scatter and a subsequent photoelectric absorption, all taking place in the GeDs. The sequence of events takes place over too small a volume to exploit time of flight for event sequence determination, so other methods are used to predict the true sequencing (Zoglauer 2005). A sequenced Compton event uniquely specifies a Compton cone whose surface represents the possible points of origin of the photon. After event reconstruction, Compton events are used in high level analysis such as List Mode Maximum Likelihood Expectation Maximization (LM-MLEM) imaging (Wilderman et al. 1998) and polarization analysis.

The predecessor to COSI was named the Nuclear Compton Telescope (NCT). NCT was flown from Ft. Sumner, New Mexico in 2005 (Boggs et al. 2006) and 2009 (Bandstra et al. 2009). The 2009 flight yielded an image of the Crab nebula, which was the first image of an astrophysical source using a compact Compton telescope (Bandstra et al. 2011). Between 2010 and 2014, our collaboration developed COSI which is upgraded in several important ways: 1) A mechanical cryocooler replaced the liquid nitrogen cooling system, thus lifting the constraint of a cryogen-limited flight duration, 2) two more GeDs were added and a new GeD arrangement of $2 \times 2 \times 3$ was chosen so as to optimize the polarization response, 3) the BGO ACS was replaced with a CsI ACS, 4) a lighter weight gondola was constructed to match the lift specification of the SPB, and 5) the previous pointing system was retired in favor of a passive zenith pointing strategy. In its current configuration, COSI’s field of view spans $\sim 25\%$ of the sky¹. In December of 2014, COSI was launched on a SPB from McMurdo Station, Antarctica. The instrument performed well and successfully measured the background environment for 36 hours, at which point a leak in the balloon was discovered, effectively ending the flight prematurely. The payload was successfully recovered, rebuilt, and launched again from Wanaka, New Zealand on 2016 May 16 (Kierans et al. 2017). For 46 days, COSI floated at a nominal altitude of ~ 33 km, continuously observing and telemetering all Compton events in real-time over the Iridium satellite network. Finally, on 2016 July 5, COSI made a relatively gentle landing in the Atacama desert of Peru. Recovery efforts were successful, including the recovery of the solid state drives containing the full raw data set.

2.1. Data Pipeline and Simulations

As photons interact in the COSI detector system, they deposit varying amounts of energy under various strips of the GeDs. The readout electronics record the x and y strip IDs, pulse heights (energy), and timing (interaction depth) of triggered events and forward these data to the flight computer for storage, real-time analysis, and telemetry. Simulating the measurement process is crucially important for benchmarking instrument performance, as well as determining instrumental responses. Thus, we used GEANT4 (Agostinelli et al. 2003) via the software library MEGALib (Zoglauer et al. 2006) to perform Monte Carlo (MC) simulations of particles propagating through a realistic mass model of the COSI instrument. Sleator et al. (2017) contains a complete description of the COSI data pipeline. The pipeline is largely the same for measured data and simulated data, with the exception that the simulated data are processed by the “detector effects engine” (DEE) (Sleator et al. 2017) before passing through the calibration modules. The goal of the DEE is to add as much realism (noise, thresholds, electronics limitations, etc.) as possible to the idealized simulation events. This way, measurements may be benchmarked against simulations. At the end of the pipeline, the events – measured or simulated – have been reconstructed and are ready for use in high level analysis.

Data analysis proceeds by imposing event selections which act to reduce background, increase signal, and optimize imaging, spectral, or polarization performance. The most relevant event selections for polarization analysis are as follows:

1. Total photon energy. All energy deposits are summed to get the total photon energy. It is possible for a photon to escape the detector system without depositing all of its energy, but these events can be identified with reasonable certainty and are rejected during event reconstruction.
2. First Compton scattering angle. This is the Compton scattering angle of the first interaction, and is determined by evaluating the classic Compton scattering formula with the total photon energy and the photon energy after the first Compton scatter.
3. Angular resolution measure (ARM). This quantity is defined as the smallest angular distance between an event’s Compton cone and a position in the sky. It is essentially an imaging cut and is applied in order to extract events whose Compton cones are consistent with a location in the sky. ARM values can be positive or negative, depending on whether the source location falls outside (positive) or inside (negative) the Compton cone.
4. Distance between first two interactions. Events with large distances are less affected by the GeD position uncertainty and generally yield lower (better) ARM values.
5. Distance between any two interactions. Events with interactions that are too close are harder to reconstruct properly, so this cut acts to improve the reconstruction efficiency.

¹ The field of view is limited by the CsI ACS, which is required for background suppression. Without the ACS, the field of view would be 4π steradians.

6. Number of interaction sites. This parameter impacts the reconstruction efficiency, since events with more interaction sites can generally be reconstructed more accurately. Events with two interaction sites are the most common, followed by three sites, four sites, etc.

Any other event parameter that is not present in this list was not used for event selection.

3. GRB 160530A

On May 30, 2016, 14 days into the flight, COSI detected the bright, long duration gamma-ray burst GRB 160530A (Tomsick & the COSI team 2016). At the time, COSI’s geographic coordinates were $\text{lat} = -56.79^\circ$, $\text{lon} = 82.31^\circ$, which resulted in a high background level due to the proximity of the South Magnetic Pole. Additionally, a relativistic electron precipitation event (REP) (Parks et al. 1979) coincided with the GRB observation, resulting in low-frequency variations in the background count rate.

Two COSI images of GRB 160530A are shown in Figure 1, where the top image corresponds to a simple back-projection of the Compton cones, and the bottom image corresponds to the same image after 10 iterations of the LM-MLEM algorithm. The images were made using 834 events with event selections that were optimized for imaging performance. The peak value in the image occurs at $l = 243.4^\circ$, $b = 0.4^\circ$ (1.5° error circle, 90% confidence), which is the best known localization for this GRB². In the local COSI coordinate frame, the GRB was 43.5° off-axis with an azimuth of -66.1° , although a gradual azimuthal motion due to an anomaly in the gondola rotator caused the GRB position to shift in the local frame by approximately 1.7° over the duration of the GRB. The average position in the local frame was used when performing simulations of GRB 160530A.

GRB 160530A was detected by Konus-Wind and INTEGRAL/ACS (Svinkin et al. 2016a), as well as Astrosat/CZTI and the CsI shield system for Astrosat/CZTI (private communication). Konus and INTEGRAL/ACS are constituents of the Inter-Planetary Network (IPN), a network of gamma-ray detectors scattered around the solar system which use time delays for source triangulation. IPN carried out a partial triangulation of GRB 160530A using the time delay between the Konus and INTEGRAL/ACS lightcurves. With only two IPN instruments detecting this GRB with a large baseline, IPN was only able to localize the source position to an annulus in the sky. The 1.5° radius COSI error circle (90% confidence) was found to overlap a region of the IPN annulus, as can be seen in Svinkin et al. (2016a). This prompted the COSI team to trigger a Swift target of opportunity observation to tile the overlapping region in search of the GRB afterglow between 19 ks and 158 ks post-burst (Evans 2016; D’Elia et al. 2016b,a). Unfortunately, Swift/XRT did not detect any fading X-ray sources, and therefore no afterglow was detected. This could be due to several reasons, the most likely being that the reported COSI error circle in Tomsick & the COSI team (2016) was not accurate at the time, and that improvements in the data pipeline since then would give a better position. We note that our updated position of $l = 243.4^\circ$, $b = 0.4^\circ$ still overlaps with the IPN annulus, but that the image in Svinkin et al. (2016a) is no longer up to date.

Figure 2 shows the COSI and Konus 50 - 200 keV light curves (top), as well as the COSI 100 - 1000 keV Compton event light curve (bottom). The light curve is characterized by two phases: a decaying pulse train lasting ~ 16 seconds, and an ensuing period of low-level activity lasting ~ 21 seconds. The pulse train is clearly visible in all three light curves, while the low-level activity is only clearly detected in the Konus data. As a result, we excluded the low-level activity phase from our analysis and only used the six pulses that are clearly seen in the COSI Compton event light curve. We performed a time domain optimization of the Compton event light curve in order to extract signal from the pulses and reject background from between the pulses. The procedure for this was to define six time windows bracketing the main pulses, and then use the Differential Evolution algorithm (Storn & Price 1997) to find the window start and end times that optimize the significance $S/\sqrt{S+B}$, where B is the expected number of background counts and S is the estimated number of source counts. The quantity B is estimated by calculating the average background count rate from two 200 second time periods bracketing the GRB, and multiplying the background rate by the total time spanned by the windows. Subtracting B from the total number of counts within the time windows yields S . The optimized time windows are shown as the grey regions in the bottom panel of Figure 2, and printed in Table 1. The total time spanned by the optimized windows is 12.945 seconds.

The time delay between the COSI light curve and the Astrosat/CZTI shield light curve was used to constrain COSI’s absolute timing accuracy. COSI events are time tagged using a 10 MHz oscillator and then converted to an absolute

² This position is different than the position originally reported in Tomsick & the COSI team (2016) of $l = 243.9^\circ$, $b = 2.1^\circ$ due to changes and improvements in the event reconstruction algorithm.

Pulse	Start Time	Stop Time
1	27.845	30.286
2	30.650	32.374
3	32.607	34.653
4	34.738	35.825
5	36.518	37.826
6	39.731	44.070

Table 1. Optimized time windows in units of seconds. Times are with respect to UTC = 1464591800 seconds (May 30th, 2016 07:03:20 UTC). The total time spanned by the windows is 12.945 seconds.

time using the pulse-per-second signal from a GPS receiver. In theory, the absolute timing accuracy of the system is $< 1\mu\text{s}$. However, calibrating the timing accuracy to this precision is challenging, and systematic effects will worsen this figure. The best fit time delay between COSI and the Astrosat/CZTI shield was 1 ± 5 ms (K. Hurley, private communication), with COSI detecting the GRB earlier. Using the position of the COSI and Astrosat instruments along with the best known COSI position for GRB 1605030A, the time delay should be 5 ms, with Astrosat detecting the burst first. Given that the absolute timing accuracy of Astrosat is known to be 2 ± 0.3 ms (D. Bhattacharya, private communication), the difference between the observed and predicted time is then 6 ± 5 ms, where the time uncertainties have been added in quadrature. Therefore, We conclude that that the absolute timing accuracy of COSI is good to 11 ms at a confidence level of 1σ .

The Konus team performed a spectral analysis of GRB 160530A on 38.9 seconds of data between 20 keV and 5 MeV (Svinkin et al. 2016b). Fitting with a Band model yielded $\alpha = -0.93 \pm 0.03$, $E_p = 638_{-33}^{+36}$ keV, and an upper limit on β , $\beta < -3.5$ (errors are 90 % confidence). The 20 keV to 10 MeV fluence was reported to be $1.30 \pm 0.04 \times 10^{-4}$ erg cm^{-2} . For our MC simulations of GRB 160530A, we used the best fit Konus Band model (Band et al. 1993) with $\beta = -3.5$, along with a multiplicative absorption model to account for extinction in the atmosphere. The effective column density was determined by integrating the NRLMSISE00 (Picone et al. 2002) model along the line of sight towards the GRB through a spherical atmosphere out to an altitude of 100 km. The result was an effective column density of 9.2 g cm^{-2} . A spectral analysis of GRB 160530A using the COSI data set will be presented elsewhere (Sleator et al., in preparation).

4. POLARIMETRIC ANALYSIS

The method for measuring the polarization level and angle of a beam in the Compton regime (100 keV to 10 MeV) – where the GRB prompt emission energy output peaks – is referred to as Compton polarimetry. When a photon Compton scatters, the scattered photon is more likely to scatter in a direction that is perpendicular to the incident photon’s electric field vector (Lei et al. 1997). In other words, if η is the azimuthal scattering angle, where $\eta = 0^\circ, 180^\circ$ corresponds to scattering along the electric field vector, then the photon preferentially scatters such that $\eta = -90^\circ$ or $+90^\circ$. Therefore, a Compton polarimeter must be able to localize the first and second interaction locations so that the azimuthal scattering angle can be measured geometrically. For a polarized beam, some fraction of the photons will have their electric field vectors aligned with a specific orientation, and so the statistical distribution of the azimuthal scattering angle is used to infer the polarization level and angle of the beam.

Two different methods were used to determine the polarization level and angle of GRB 160530A: a standard method (SM), where the azimuthal scattering angles are histogrammed and then fit with a “modulation” curve, and a maximum likelihood method (MLM) which does not bin the data and uses more information per photon. A detailed description of our implementation of the MLM can be found in the accompanying paper “Maximum Likelihood Compton Polarimetry with the Compton Spectrometer and Imager,” hereafter referred to as P2 (Lowell et al. 2017, submitted).

Event Selections

Total photon energy	111 – 847 keV
First Compton scattering angle	55.4° – 145.2°
Angular resolution measure	ARM < 12.5°
Smallest distance between first two interactions	0.5 cm
Smallest distance between any two interactions	0.3 cm
Number of interaction sites	2 - 7

Statistics

Total counts T	445
Background counts B	123
MDP	72.3 ± 0.8%
Modulation factor μ_{100}	0.484 ± 0.002

Fit Results

Amplitude (counts s ⁻¹)	0.12 ± 0.08
Offset (counts s ⁻¹)	0.76 ± 0.05
Fitted polarization angle $\hat{\eta}_0$	117 ^{+19°} _{-20°}
Fitted modulation $\hat{\mu}$	0.16 ^{+0.16} _{-0.15}
Polarization level $\Pi = \hat{\mu}/\mu_{100}$	33 ^{+33%} _{-31%}
Π 90% upper limit	79%
χ^2_{red} (dof = 27)	0.98

Table 2. SM event selections, statistics, and fit results. The number of bins in the azimuthal scattering angle distribution was 30 (12° per bin).

4.1. Standard Method

The polarization level and angle are determined in the SM by fitting the following function to the azimuthal scattering angle distribution:

$$F - A \cos(2(\eta - \eta_0)), \quad (1)$$

where F is the offset, A is the amplitude, and η_0 is the polarization angle. During the χ^2 minimization, A , F , and η_0 are left free. The measured modulation $\hat{\mu}$ is defined as $\hat{\mu} = A/F$. To convert the measured modulation to a polarization level, $\hat{\mu}$ must be divided by the modulation factor μ_{100} , which is the modulation in the case that the source is 100% polarized.

The first step in the SM is to determine the event selections that optimize the statistical minimum detectable polarization (Weisskopf et al. 2010; Strohmayer & Kallman 2013):

$$\text{MDP} = \frac{4.29}{\mu_{100} r_s} \cdot \sqrt{\frac{r_s + r_b}{t}}, \quad (2)$$

where r_s is the average source count rate, r_b is the average background count rate, and t is the observation time. The factor of 4.29 in Equation 2 corresponds to a confidence level of 99%. During the optimization, the observation time t was fixed at 12.945 seconds (from the time domain optimization), while r_s , r_b , and μ_{100} were computed for various energy, Compton scattering angle, and ARM selection ranges. For each ensemble of event selections, r_s and r_b were computed using the real data, while μ_{100} was computed using a polarized simulation of GRB 160530A with an

arbitrary polarization angle. We employed the Differential Evolution optimization algorithm to find the energy range, Compton scattering angle range, and ARM cut that optimize Equation 2. It is reasonable to expect the range on the Compton scattering angle to close in towards $\sim 90^\circ$, as this is where the ideal modulation peaks (Lei et al. 1997), giving a larger value for μ_{100} . However, a trade-off exists between the magnitude of μ_{100} and the source count rate; the optimized event selections should give as large a value for μ_{100} as possible while still accepting as many source counts as possible. The other event selections – distance between interactions, and number of interaction sites – were fixed during the optimization. The first distance cut was set to 0.5 cm so as to avoid artifacts that appear in the azimuthal scattering angle distributions when the interactions are too close. These artifacts are a result of the finite position resolution of the detectors. The cut on the minimum distance between any two interactions was set at a more relaxed 0.3 cm, which has the effect of rejecting many 3+ site events where interactions occur on neighboring strips (strip pitch = 0.2 cm). This has no impact on the azimuthal scattering angle measurement, since the azimuthal angle is only measured using the first two interactions which are subject to the more restrictive 0.5 cm cut. Finally, events with two or more interaction sites were used in order to get as many counts as possible, although no events were detected with more than five interaction sites. Table 2 shows the event selections used for the SM.

After applying these selections, $T = 445$ total counts remained for the analysis, approximately $B = 123$ of which were background. The number of background counts B was estimated by fitting a third order polynomial to the light curve 200 seconds before and after the GRB, but with the time bins corresponding to the GRB excluded from the fit. Integrating the polynomial over the optimized time windows resulted in $B = 123$. Using Equation 2 and assuming no systematic error, the MDP was $58 \pm 2\%$. In order to determine the MDP including systematic errors, we generated $N = 10,000$ trial data sets using $S = T - B = 322$ counts from an unpolarized simulation of GRB 160530A, and $B = 123$ counts from real background events taken from two 200 second intervals bracketing the GRB. For each trial data set, the polarization analysis was performed and the resulting polarization level was stored. Finally, the 99th percentile of polarization levels was determined numerically and found to be $\text{MDP} = 72.3 \pm 0.8\%$. We used this value as our 99% confidence (2.6σ) detection threshold.

We studied the dependence of the modulation factor μ_{100} on the polarization angle by performing MC simulations of a 100% polarized GRB 160530A at various polarization angles. The result of each simulation is shown in Figure 3, along with the best fit constant. The χ_{red}^2 for the fit is 0.42 (dof = 17), indicating that the value of μ_{100} is consistent with being uniform over the full range of polarization angles. The best fit constant $\mu_{100} = 0.484 \pm 0.002$ was used in the following analysis.

Once the best event selections and μ_{100} have been identified, the SM analysis may proceed. Three separate azimuthal scattering angle distributions (ASADs) are shown in Figure 4, corresponding to a background subtracted ASAD for GRB 160530A (top), a “correction” ASAD generated from an unpolarized simulation of GRB 160530A (middle) which has been rescaled by the mean value, and finally the corrected ASAD with the best fit modulation curve (bottom). The final corrected ASAD (bottom) was obtained by dividing the background-subtracted GRB 160530A ASAD (top) by the “correction” ASAD (middle). This was done to correct for systematic effects of the detector system such as non-uniformity of efficiency (due to geometry, channel thresholds, etc.) and measurement uncertainty. The fit results are shown in Table 2. We measured a polarization level of $\Pi = 33_{-31}^{+33}\%$ for this GRB using the SM, which was below the detection limit $\text{MDP} = 72.3 \pm 0.8\%$. In order to determine the 90% confidence upper limit on the polarization level, we used the MINOS (James & Roos 1975) algorithm to determine the 90% confidence contour in the 2D parameter space of amplitude vs. offset. Then, the maximum value for the modulation along the contour was found and divided by μ_{100} , which yielded a 90% upper limit on the polarization level of 87%.

4.2. Maximum Likelihood Method

The MLM aims to determine the polarization level Π and angle η_0 that maximize the log likelihood:

$$\ln \mathcal{L} = \sum_{i=1}^N \ln p(\eta_i; E_i, \theta_i, \Pi, \eta_0), \quad (3)$$

where N is the number of events, and p is the probability³ of measuring the azimuthal scattering angle η_i , given that the energy E_i and Compton scattering angle θ_i of event i have been accurately measured, and that the polarization level

³ For more details on the functional form of the probability distributions used in the MLM, please refer to P2.

and angle are Π and η_0 , respectively. The values of Π and η_0 that maximize the log likelihood for a given observation are defined as $\hat{\Pi}$ and $\hat{\eta}_0$, where $\hat{\Pi}$ is referred to as the uncorrected polarization level. The corrected polarization level is given by:

$$\Pi = \frac{\hat{\Pi}}{\Pi_{100}}, \quad (4)$$

where Π_{100} is the MLM correction factor, defined such that $\Pi_{100} = \hat{\Pi}$ when the true polarization level is $\Pi = 100\%$ and the number of background counts B is zero. An ideal polarimeter with perfect reconstruction efficiency and no measurement error would have $\Pi_{100} = 1$. Figure 5 shows Π_{100} for COSI as a function of polarization angle from MC simulations of GRB 160530A. As in the SM case, the distribution is rather uniform; the best fit constant has a value of $\Pi_{100} = 0.799 \pm 0.003$ with a χ_{red}^2 of 0.65 (dof = 17). Once again, we used the best fit constant for the MLM analysis.

In the presence of background, the probability distribution in Equation 3 must be mixed with the probability distribution which describes the background, p_{bkg} . The relative contributions of the source and background probability are mixed using the signal purity $f = (T - B)/T$, where T is the total number of counts, and B is the expected number of background counts. The total probability⁴ for event i is then:

$$p_{total} = f \cdot p(\eta_i; E_i, \theta_i, \Pi, \eta_0) + (1 - f) \cdot p_{bkg}(\eta_i; E_i, \theta_i), \quad (5)$$

For the event selections in Table 3, we compute a signal purity of $f = 0.72 \pm 0.01$. The error bar on the signal purity is the standard deviation of the simulated distribution of f , obtained by randomly sampling the Poisson distributions underlying T and B . We determined p_{bkg} by accumulating background events from a time period which included GRB 160530A. Due to the large number of bins (46656) in the histogram representing p_{bkg} , this time period spanned 48 hours (7 hours pre-GRB, 41 hours post-GRB). Although it would have been preferable to only include background data from a time period closer in time to the GRB itself, this was not possible due to the relatively low absolute count rate. The background environment at balloon float altitudes, which is dominated by cosmic ray secondaries (photons in particular), is known to vary with altitude, or equivalently, atmospheric depth (Ling 1975; Bowen et al. 2007). Throughout the 48 hour background integration interval, the COSI altitude was quite stable at ~ 33.1 km, with small excursions at a level of $< 2\%$. Thus, we conclude that using background events from this time interval is a reasonable choice.

The MLM can perform better than the SM because additional information – the photon energy and Compton scattering angle – is used to implicitly weight each event’s contribution to the likelihood statistic (Krawczynski 2011). Contrast this with the SM, where the azimuthal scattering angle of each event that passes the event selections is added to a histogram, and all other event information is discarded. Additionally, the MLM benefits from being able to use events with any energy or Compton scattering angle, resulting in more usable counts for the analysis. Consequently, for the MLM event selections, we accepted all photon energies between 100 and 1000 keV, as well as all Compton scattering angles $0^\circ - 180^\circ$. With these broader selections, we determined that the FWHM of the ARM distribution was 11.9° using simulated data. For the ARM selection range, we used twice the FWHM of the ARM distribution, centered about zero, i.e. $|\text{ARM}| < 11.9^\circ$. The distance cuts used for the MLM were the same as for the SM and for the same reasons as outlined in Section 4.1.

After applying the MLM event selections, $T = 542$ counts remained for the analysis, approximately $B = 152$ of which were background. Once again, B was determined by fitting a third order polynomial to the light curve, and integrating the polynomial over the time windows (Table 1). The MDP was computed in a similar fashion to the SM, where $N = 10,000$ unpolarized trial observations were generated and analyzed using the MLM. This process yielded $\text{MDP} = 57.5 \pm 0.8\%$.

Table 3 summarizes the results of the MLM analysis, while Figure 6 shows the confidence contours for GRB 160530A along with the best fit values, detection limit, and 90% confidence upper limit. The corrected polarization level was $\Pi = 16_{-16}^{+27}\%$, which was below the detection limit $\text{MDP} = 57.5 \pm 0.8\%$. We obtained a 90% confidence upper limit on the corrected polarization level Π using a Monte Carlo/bootstrap approach. The procedure was as follows. First we generated $N = 10,000$ bootstrap resamples of the measured data. Second, for each resample, we drew a value of $f = (T - B)/T$ by assuming a Poisson distribution for the total number of counts ($T = 542$) and the expected number

⁴ See footnote 3.

Event Selections

Total photon energy	100 - 1000 keV
First Compton scattering angle	$0^\circ - 180^\circ$
Angular resolution measure	$ \text{ARM} < 11.9^\circ$
Smallest distance between first two interactions	0.5 cm
Smallest distance between any two interactions	0.3 cm
Number of interaction sites	2 - 7

Statistics

Total counts T	542
Background counts B	152
Signal purity f	0.72 ± 0.01
MDP	$57.5 \pm 0.8\%$
MLM correction factor Π_{100}	0.799 ± 0.003

Fit Results

Fitted polarization angle $\hat{\eta}_0$	$141^\circ \pm 47^\circ$
Fitted, uncorrected polarization level $\hat{\Pi}$	$0.13^{+0.22}_{-0.13}$
Corrected polarization level $\Pi = \frac{\hat{\Pi}}{\Pi_{100}}$	$16^{+27}_{-16} \%$
Π 90% upper limit	46%

Table 3. MLM event selections, statistics, and fit results.

of background counts ($B = 152$). Third, we re-ran the minimizer on each resample using the value of f generated in step 2 in order to yield a value of $\hat{\Pi}$. Finally, the $\hat{\Pi}$ values were re-scaled by values of Π_{100} drawn from its associated probability distribution, which was assumed to be Gaussian. The 90th percentile of the resulting distribution on Π was then used as the 90% confidence upper limit. Using this procedure, we arrived at a 90% confidence upper limit of 46% on the polarization level. The benefit of the Monte Carlo/bootstrap approach is that the errors in the signal purity and Π_{100} are correctly propagated into the final result.

5. DISCUSSION

Both the SM and MLM give best fit polarization levels below their respective MDPs, so we conclude that COSI did not detect polarized emission from GRB 160530A at a confidence level of 99%. Moreover, from the error bars on the polarization levels, as well as the log likelihood contours, the measured polarization level is consistent with $\Pi = 0\%$ at a confidence level of 1σ . Our most constraining 90% confidence upper limit on the polarization level was 46% using the MLM. This upper limit is not strong enough to favor or disfavor any particular polarization scenario on its own. However, several GRBs have been found to be polarized at a level above our upper limit (McConnell 2017), so our result is indeed useful in the context of the overall distribution of polarization levels within the GRB population. GRBs with polarization levels exceeding $\Pi = 46\%$ can be generated in the Compton drag model (Lazzati et al. 2004), but are more frequently explained as arising from a scenario where synchrotron emission in an ordered magnetic field dominates. However, the polarization level in such scenarios can be reduced to lower levels due to certain factors, such as an evolution in the polarization angle with time. Such changes in the polarization angle with time were seen in GRB 100826A (Yonetoku et al. 2011b), and it has been theorized that each pulse in a GRB light curve may correspond to a distinct ordering – and thus polarization angle – of a large scale magnetic field within the GRB jet. Moreover, the Internal-Collision-induced MAGnetic Reconnection and Turbulence (ICMART) model for GRBs (Zhang & Yan 2011) predicts that the polarization angle and level change from pulse to pulse, and also that the polarization level continually

decreases throughout the duration of each pulse. These changes in the polarization properties with time are theorized to result from collisions between highly magnetized shells, which are launched intermittently from the GRB central engine. As the shells collide, the magnetic field lines distort and lose uniformity, thus reducing the polarization level of synchrotron emission. GRB 160530A, whose early phase light curve is composed of several clear pulses, would be a good candidate to perform time-resolved polarimetry. Unfortunately the number of counts detected with COSI from this GRB was not large enough to enable such studies.

Several factors reduced COSI's sensitivity to this GRB. First, attenuation by the atmosphere significantly reduced the source flux; at the average measured photon energy of 360 keV, and with an effective column density of 9.2 g cm^{-2} , approximately 60% of photons were absorbed or scattered by the atmosphere. Moreover, the 100 - 1000 keV flux of the Band model with the atmospheric absorption component is reduced by 64% compared to the unabsorbed case. Second, the GRB occurred 43.5° off axis in the COSI local frame, so the effective area was reduced by about 22% due to occultation from the CsI shields. Third, by the time COSI detected this GRB, two germanium detectors were no longer operational due to anomalies in the corresponding high voltage supplies. Accordingly, all MC simulations discussed in this paper treated the two non-functioning detectors as passive mass. A simulation of the fully functioning detector system revealed that about 16% of events were lost due to the malfunctioning detectors. Lastly, as mentioned in Section 3, the GRB coincided with a REP event as well as a relatively close approach to the South Magnetic Pole, both of which had the effect of elevating the background count rate.

Despite these losses, we were able to regain some sensitivity by using the maximum likelihood based approach. Notably, the MDP in the MLM is $\sim 20\%$ lower than the SM, while the 90% confidence upper limit on the polarization level is $\sim 42\%$ lower. This improvement in MDP is consistent with what was reported by Krawczynski (2011), where the MDP of an idealized Compton polarimeter was shown to improve by $\sim 21\%$ when using the MLM.

6. ACKNOWLEDGEMENTS

The authors would like to thank: Jamie Kennea and Phil Evans of the Swift team for their help with analysis of the Swift/XRT follow up observations; Kevin Hurley and the IPN team for their efforts to triangulate GRB160530A, which helped plan the Swift/XRT observations; Varun Bhalerao and Dipankar Bhattacharya with the Astrosat team for helping us cross-calibrate COSI's timing performance with Astrosat; the NASA Columbia Scientific Ballooning Facility team for successfully flying (and landing) COSI and making this work possible. COSI is funded by NASA grant NNX14AC81G-APRA. Swift Guest Observer analysis is supported through NASA grant NNH15ZDA001N-SWIFT. This work is also supported in part by CNES.

Software: GEANT4 (Agostinelli et al. 2003), MINUIT (James & Roos 1975), MEGALib (Zoglauer et al. 2006), ROOT (Brun & Rademakers 1997)

REFERENCES

- Agostinelli, S., Allison, J., Amako, K., et al. 2003, Nuclear Instruments and Methods in Physics Research Section A: Accelerators, Spectrometers, Detectors and Associated Equipment, 506, 250 .
<http://www.sciencedirect.com/science/article/pii/S0168900203011064>
- Amman, M., Luke, P., & Boggs, S. 2007, Nuclear Instruments and Methods in Physics Research Section A: Accelerators, Spectrometers, Detectors and Associated Equipment, 579, 886 .
<http://www.sciencedirect.com/science/article/pii/S0168900207011064>
- Band, D., Matteson, J., Ford, L., et al. 1993, ApJ, 413, 281
- Bandstra, M. S., Bellm, E. C., Chiu, J.-L., et al. 2009, in Nuclear Science Symposium Conference Record (NSS/MIC), 2009 IEEE, IEEE, 2131–2139
- Bandstra, M. S., Bellm, E. C., Boggs, S. E., et al. 2011, ApJ, 738, 8
- Bhalerao, V., Bhattacharya, D., Vibhute, A., et al. 2017, Journal of Astrophysics and Astronomy, 38, 31.
<https://doi.org/10.1007/s12036-017-9447-8>
- Boggs, S., Bandstra, M., Bowen, J., et al. 2006, in Focusing Telescopes in Nuclear Astrophysics (Springer), 387–394
- Bowen, J. D., Bandstra, M. E., Boggs, S. E., et al. 2007, in 2007 IEEE Nuclear Science Symposium Conference Record, Vol. 1, 436–444
- Brun, R., & Rademakers, F. 1997, Nuclear Instruments and Methods in Physics Research Section A: Accelerators, Spectrometers, Detectors and Associated Equipment, 389, 81 , new Computing Techniques in Physics Research V.
<http://www.sciencedirect.com/science/article/pii/S0168900297001106>
- Chattopadhyay, T., Vadawale, S. V., Aarthy, E., et al. 2017, ArXiv e-prints, arXiv:1707.06595

- Chiu, J.-L., Boggs, S., Chang, H.-K., et al. 2015, Nuclear Instruments and Methods in Physics Research Section A: Accelerators, Spectrometers, Detectors and Associated Equipment, 784, 359, symposium on Radiation Measurements and Applications 2014 (SORMA XV). <http://www.sciencedirect.com/science/article/pii/S0168900214002444>
- D'Elia, V., Izzo, L., Breeveld, A. A., & Markwardt, C. B. 2016a, GRB Coordinates Network, 19501
- D'Elia, V., Izzo, L., Evans, P. A., et al. 2016b, GRB Coordinates Network, 19481
- Evans, P. A. 2016, GRB Coordinates Network, 19472
- Granot, J. 2003, Astrophysical Journal, 596, L17. www.scopus.com
- Gruzinov, A., & Waxman, E. 1999, ApJ, 511, 852
- James, F., & Roos, M. 1975, Computer Physics Communications, 10, 343
- Kierans, C. A., Boggs, S. E., Chiu, J.-L., et al. 2017, ArXiv e-prints, arXiv:1701.05558
- Kole, M., & Marcinkowski, R. 2016, GRB Coordinates Network, 20301
- Kole, M., Produit, N., Bernasconi, T., et al. 2016, GRB Coordinates Network, 20243
- Krawczynski, H. 2011, Astroparticle Physics, 34, 784
- Lazzati, D., Rossi, E., Ghisellini, G., & Rees, M. J. 2004, Monthly Notices of the Royal Astronomical Society, 347, L1. [+http://dx.doi.org/10.1111/j.1365-2966.2004.07387.x](http://dx.doi.org/10.1111/j.1365-2966.2004.07387.x)
- Lei, F., Dean, A., & Hills, G. 1997, Space Science Reviews, 82, 309
- Ling, J. C. 1975, J. Geophys. Res., 80, 3241
- Lowell, A., Boggs, S., Chiu, J. L., et al. 2016, Positional calibrations of the germanium double sided strip detectors for the Compton spectrometer and imager, , , doi:10.1117/12.2233145. <http://dx.doi.org/10.1117/12.2233145>
- Lyutikov, M., Pariev, V. I., & Blandford, R. D. 2003, Astrophysical Journal, 597, 998. www.scopus.com
- McConnell, M. L. 2017, New Astronomy Reviews, 76, 1. <http://www.sciencedirect.com/science/article/pii/S1387647316300495>
- Orsi, S., Cadoux, F., Leluc, C., et al. 2014, The POLAR gamma-ray burst polarimeter onboard the Chinese Spacelab, , , doi:10.1117/12.2055910. <http://dx.doi.org/10.1117/12.2055910>
- Parks, G., Gurgiolio, C., & West, R. 1979, Geophysical Research Letters, 6, 393
- Picone, J., Hedin, A., Drob, D. P., & Aikin, A. 2002, Journal of Geophysical Research: Space Physics, 107
- Produit, N., Barao, F., Deluit, S., et al. 2005, Nuclear Instruments and Methods in Physics Research Section A: Accelerators, Spectrometers, Detectors and Associated Equipment, 550, 616
- Shaviv, N. J., & Dar, A. 1995, ApJ, 447, 863
- Sleator, C. C., Boggs, S. E., Chiu, J.-L., et al. 2017, arXiv preprint arXiv:1701.05563
- Storn, R., & Price, K. 1997, Journal of Global Optimization, 11, 341. <http://dx.doi.org/10.1023/A:1008202821328>
- Strohmer, T. E., & Kallman, T. R. 2013, The Astrophysical Journal, 773, 103. <http://stacks.iop.org/0004-637X/773/i=2/a=103>
- Sun, J. C., Wu, B. B., Bao, T. W., et al. 2016, Performance study of the gamma-ray bursts polarimeter POLAR, , , doi:10.1117/12.2232133. <http://dx.doi.org/10.1117/12.2232133>
- Svinkin, D., Golenetskii, S., Aptekar, R., et al. 2016a, GRB Coordinates Network, 19476
- . 2016b, GRB Coordinates Network, 19477
- Toma, K., Sakamoto, T., Zhang, B., et al. 2009, The Astrophysical Journal, 698, 1042
- Tomsick, J. A., & the COSI team. 2016, GRB Coordinates Network, 19473
- Waxman, E. 2003, Nature, 423, 388
- Weisskopf, M. C., Elsner, R. F., & O'Dell, S. L. 2010, in Proc. SPIE, Vol. 7732, Space Telescopes and Instrumentation 2010: Ultraviolet to Gamma Ray, 77320E
- Wilderman, S. J., Clinthorne, N. H., Fessler, J. A., & Rogers, W. L. 1998, in Nuclear Science Symposium, 1998. Conference Record. 1998 IEEE, Vol. 3, IEEE, 1716-1720
- Yonetoku, D., Murakami, T., Gunji, S., et al. 2011a, Publications of the Astronomical Society of Japan, 63, 625. [+http://dx.doi.org/10.1093/pasj/63.3.625](http://dx.doi.org/10.1093/pasj/63.3.625)
- . 2011b, The Astrophysical Journal Letters, 743, L30. <http://stacks.iop.org/2041-8205/743/i=2/a=L30>
- . 2012, The Astrophysical Journal Letters, 758, L1. <http://stacks.iop.org/2041-8205/758/i=1/a=L1>
- Zhang, B., & Yan, H. 2011, The Astrophysical Journal, 726, 90. <http://stacks.iop.org/0004-637X/726/i=2/a=90>
- Zoglauer, A., Andritschke, R., & Schopper, F. 2006, NewAR, 50, 629
- Zoglauer, A. C. 2005, PhD thesis, Technische Universität München

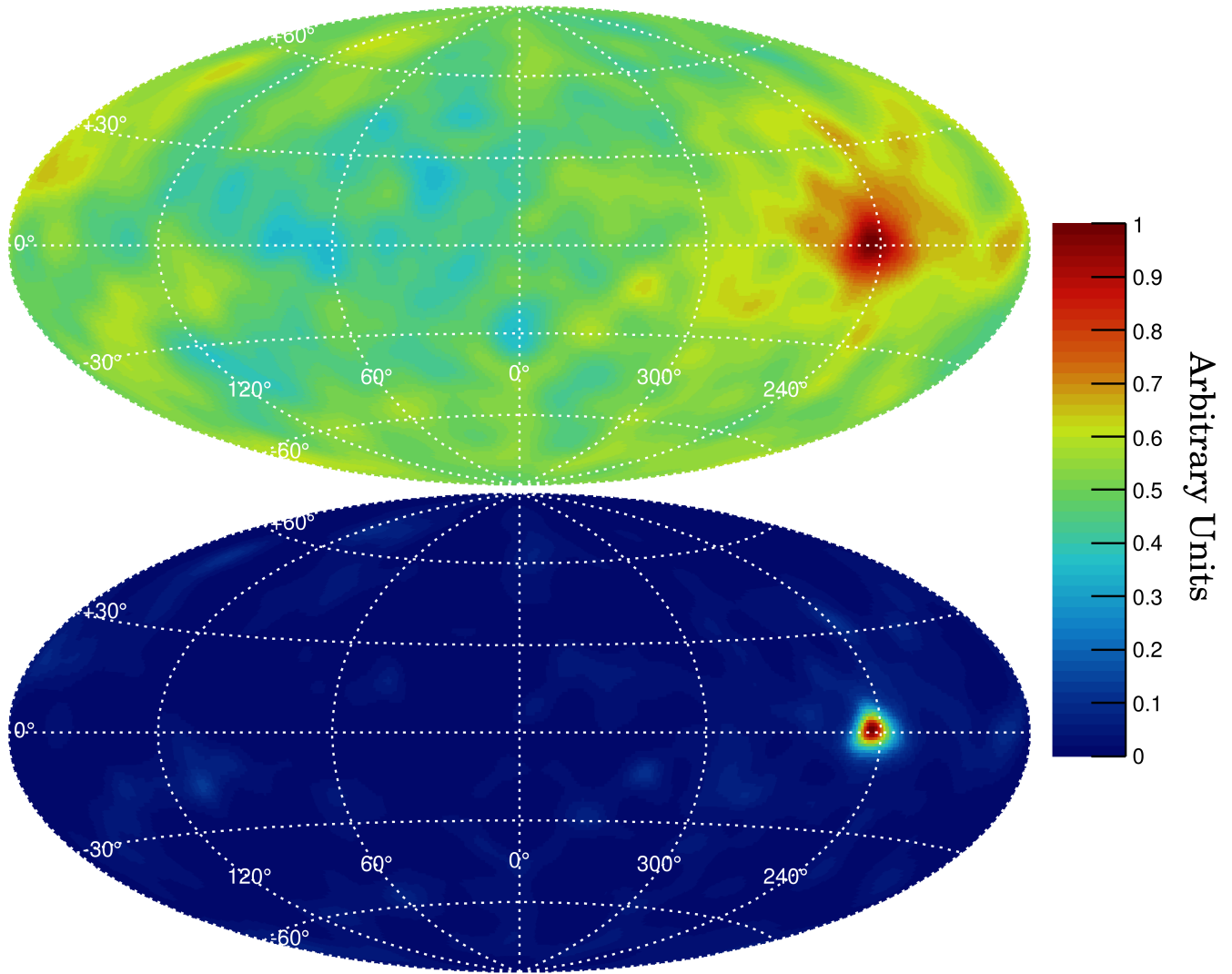


Figure 1. Two COSI images of GRB 160530A in Galactic coordinates using zero iterations (top) and ten iterations (bottom) of the LM-MLEM image deconvolution algorithm. Zero iterations corresponds to a simple back-projection of the Compton cones. The event selections used to make this image were different than those used for the polarization analysis, as the goal here is imaging performance. The color scale intensity is in arbitrary units.

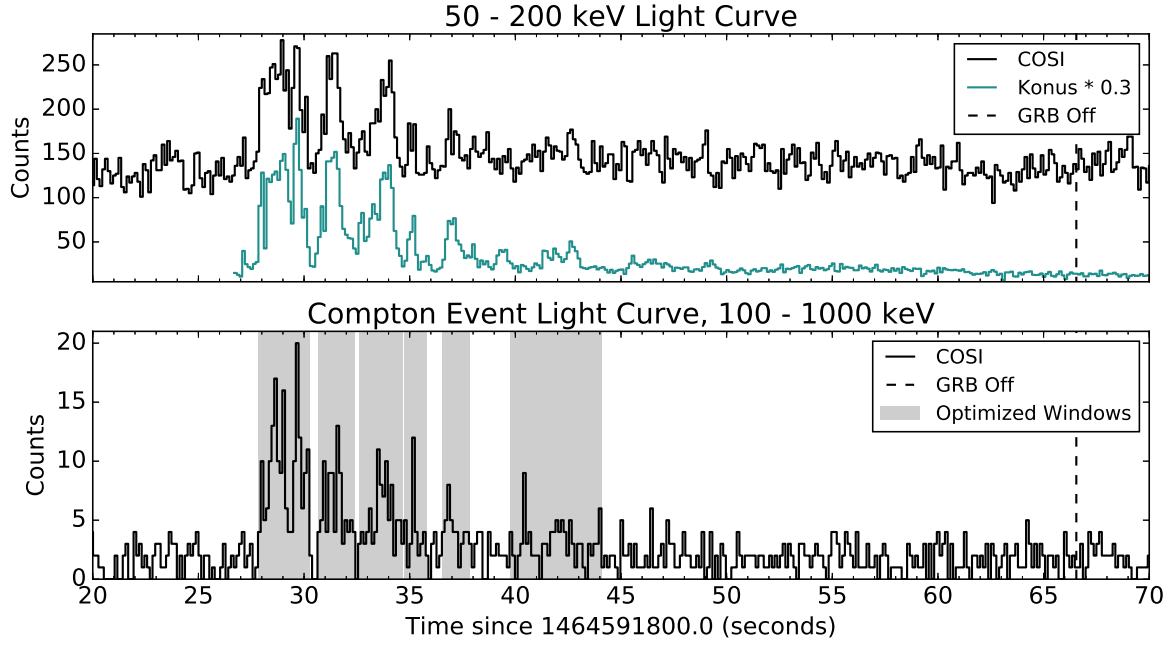


Figure 2. (top) COSI and Konus light curves plotted for photon energies between 50 and 200 keV. The Konus light curve has been shifted by +0.651 seconds to account for the COSI-Konus delay time. In this energy band, only 2% of events are Compton events; the rest are single-site events. (bottom) The COSI Compton event light curve, using the event selections shown in Table 3.

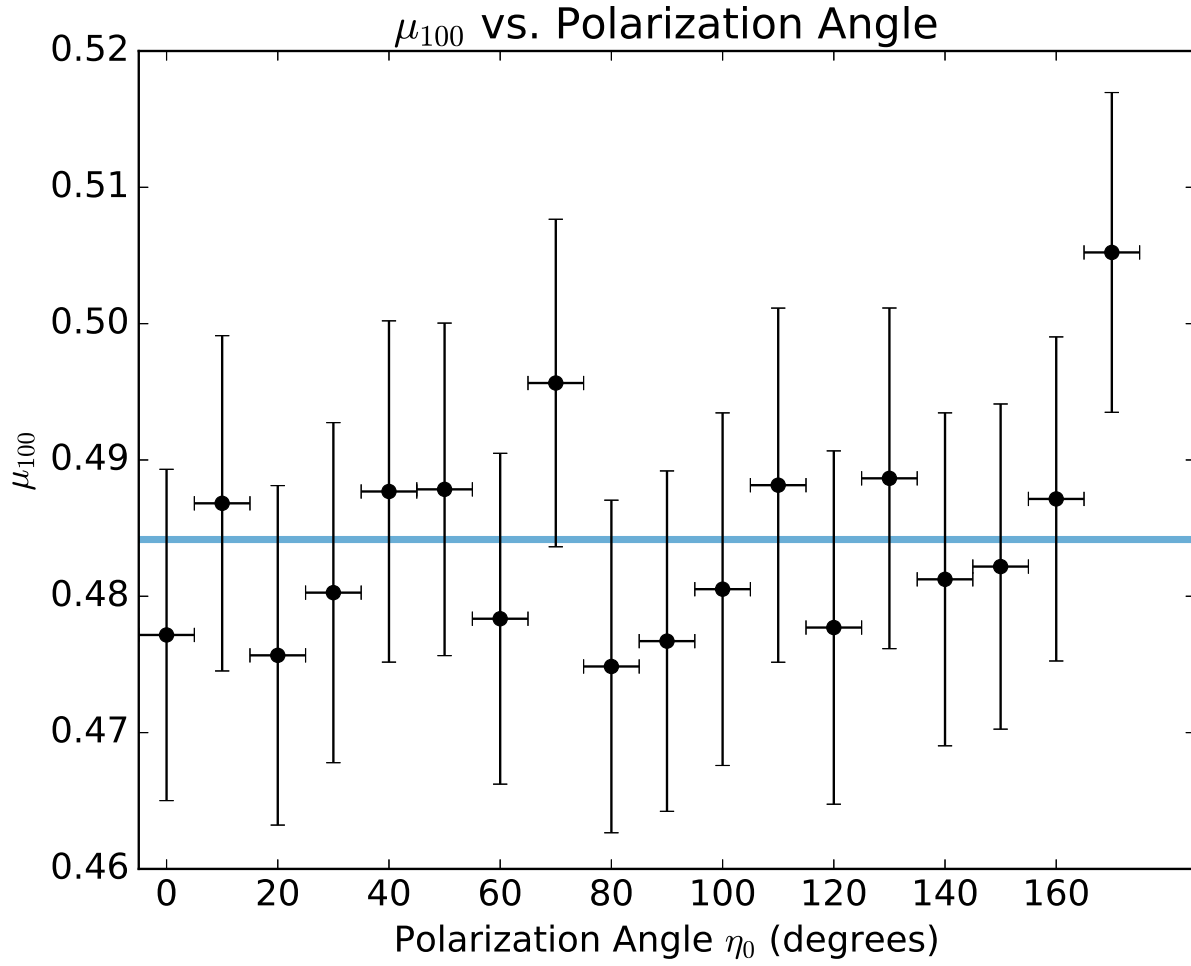


Figure 3. The modulation factor μ_{100} as a function of the simulated polarization angle, along with the best fit constant value of $\mu_{100} = 0.484 \pm 0.002$, $\chi^2_{red} = 0.42$ (dof = 17). For each simulation, $2.4 - 2.5 \times 10^4$ counts were used.

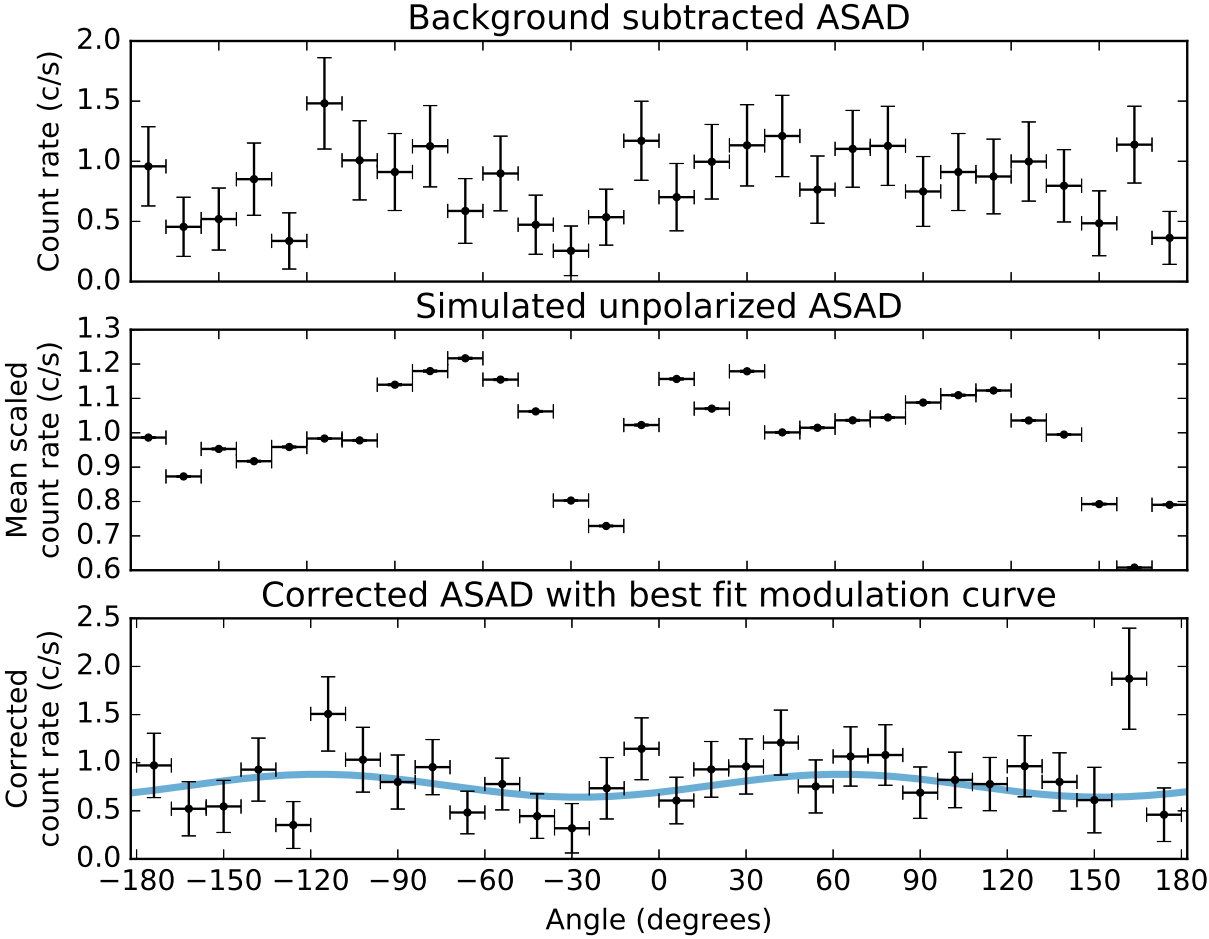


Figure 4. The background subtracted azimuthal scattering angle distribution (ASAD) for GRB160530A (top), an ASAD from an unpolarized simulation of GRB160503A used to correct for systematics (middle), and the corrected ASAD (bottom) showing the best fit modulation curve in blue.

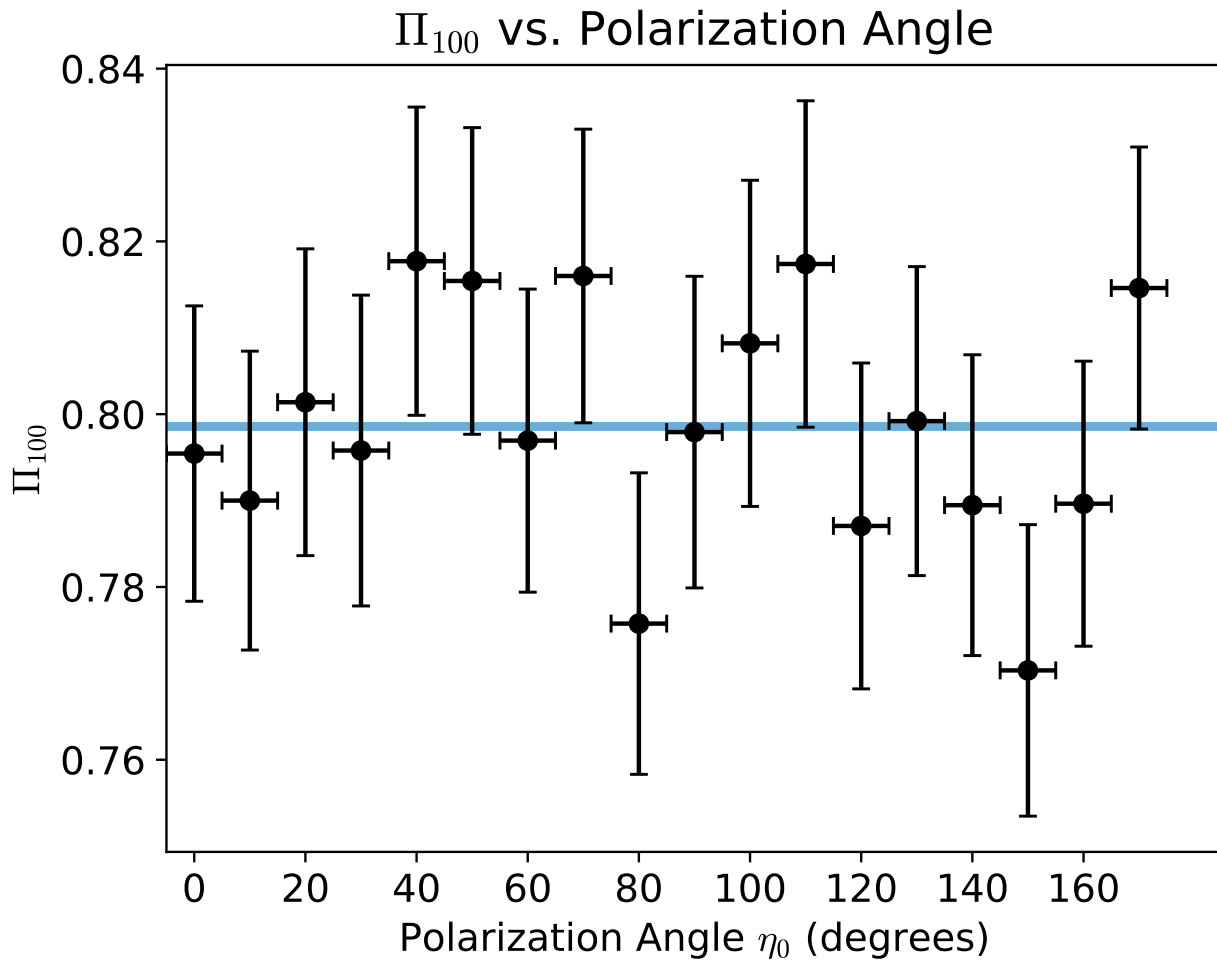


Figure 5. The MLM correction factor Π_{100} as a function of the simulated polarization angle, along with the best fit constant value $\Pi_{100} = 0.799 \pm 0.003$, $\chi_{red}^2 = 0.65$ (dof = 17). For each simulation, $3.4 - 3.6 \times 10^4$ counts were used.

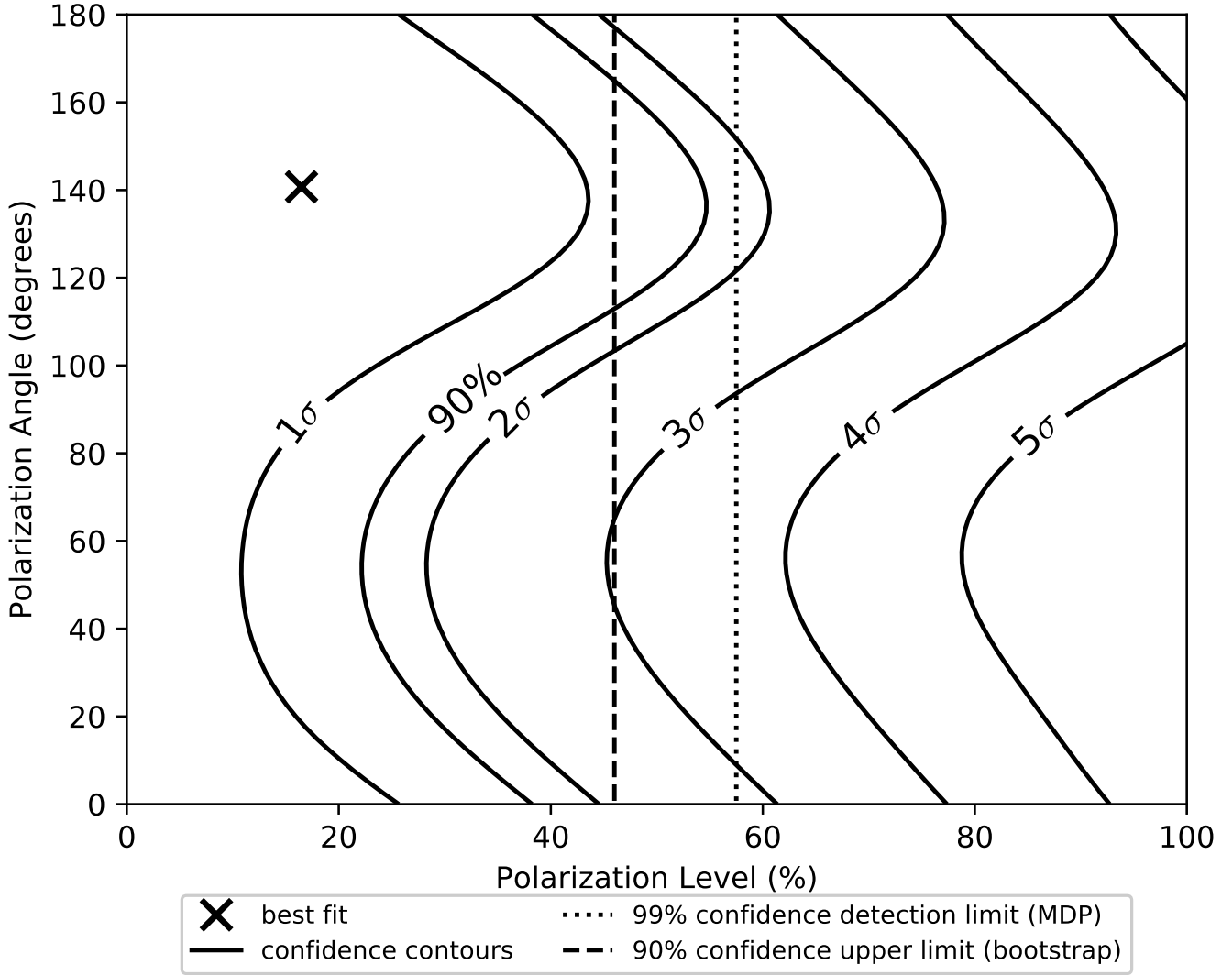


Figure 6. Confidence contours for GRB 160530A, derived from a map of the log likelihood. The optimal polarization level and angle are denoted by the cross. Confidence contours are shown for 1-5 σ as well as 90% confidence. The dashed line denotes the 90% confidence upper limit on the polarization level as determined using a Monte Carlo/bootstrap technique. The dotted line represents the MDP, or equivalently, the 99% confidence detection threshold.